Chapter 3

A radio monitoring program for southern blazars

Tyger, Tyger, burning bright,
In the forests of the night,
What immortal hand or eye
Could frame thy fearful symmetry?
William Blake, *The Tyger*

3.1 Introduction

As discussed in Section 1.2.1, comparison of variability behaviour and time-scales in different wavebands may help to constrain models of emission, and hence the geometry and physics of the inner jets of AGN. To this end, several radio monitoring programs were recently undertaken to complement observations of blazars at X-ray energies.

Between 1997 and 2000, a radio monitoring program for a sample of blazars was carried out with the Australia Telescope Compact Array (ATCA) and the Australia Telescope Long Baseline Array (LBA). The sample consists of a variety of flat-spectrum radio-loud quasars (FSRQ) and BL Lac objects, which had been selected as targets for the X-ray astronomy satellite BeppoSAX. All sources had been previously been detected at X-ray energies, although the majority are not strong X-ray sources. Fourteen out of the twenty-two sources making up the core sample are also identified with detections at γ-ray energies greater than 100 MeV, by the Energetic Gamma-Ray Experiment Telescope (EGRET) on board the *Compton Gamma-Ray Observatory (CGRO)* (e.g. Thompson et al., 1995). The sample is inhomogeneous, with sources being of individual interest for multi-wavelength studies.

The ATCA monitoring program was intended to complement a radio flux density monitoring program for 23 northern, strong radio blazars, the results of which are presented by Venturi et al. (2001). The program for the northern blazars was started in January 1996 using the 32-m antennas at Medicina (Bologna, Italy) and Noto (Siracusa, Italy). In May 1997, a similar program was commenced with the ATCA for 22 blazars from the BeppoSAX target list, including an overlapping 6 sources from the northern

sample. The ATCA has a number of advantages over the single dish telescopes, as described in Section 2.3. In particular, the ATCA program measured full polarization parameters and could include fainter sources, as well as providing instantaneous spectra at four frequencies. A major aim of both monitoring programs was to contribute to a multi-wavelength database for a large number of blazars, from which radio properties and variability can be compared with observations at X-ray and other energy bands.

The radio flux density monitoring was carried out at regular intervals, bi-monthly in the case of the ATCA program, over more than two years. The X-ray sampling, however, proved to be quite different. Not all sources in the ATCA sample were observed with BeppoSAX during the 3 years of the ATCA monitoring, and several sources were observed only once. For the few sources which have multiple X-ray observations, these were in general performed intensively over a short time period (e.g. several days or weeks). Therefore, one of the original goals of the program, which was to search for correlated variability between X-ray and radio bands, proved unachievable. However, the radio data alone are of value for investigating source properties.

A sub-sample of 12 sources selected from the ATCA sample was monitored with VLBI using the LBA. The main aims of the VLBI observations were to examine source structure on milliarcsecond scales, to constrain source brightness temperatures from component angular sizes, and also to try to detect changes in structure with time. If the separation of components can be measured in multiple epochs, then it is possible to place constraints on the intrinsic speed and angle to the line-of-sight of the jet. Apparent superluminal motion is commonly observed in blazars (e.g. Kellermann et al., 2000). The results of the VLBI observations are presented in Section 3.3, including a single epoch of observations with the NRAO's Very Long Baseline Array (VLBA) for three sources. Due to the very compact nature of these sources it was not possible to measure component separations using the LBA. Such measurements may be possible in the near future, with an improved Southern Hemisphere VLBI array.

A number of sources in the sample have been observed in other long-term radio monitoring programs overlapping in time with the Medicina/Noto and ATCA monitoring. The University of Michigan Radio Astronomy Observatory (UMRAO) has been dedicated for three decades to monitoring a large number of compact radio sources (Aller et al., 1996). The Effelsberg 100 m radio telescope has also been used to monitor flux densities of extragalactic sources over a number of years (e.g. Peng et al., 2000). Additionally, the Green Bank Interferometer (GBI) produced a large database of flux density monitoring (Lazio et al., 2001b), before its closure in 2000. However, the southernmost sources in the ATCA sample are not well studied compared with many of the sources observable from the Northern Hemisphere.

Fifteen sources out of the core sample were included in the VSOP Survey and were part of another ATCA program which monitored flux densities of all of the southern VSOP Survey sources, over a similar time period as the blazar monitoring presented in this chapter (Tingay et al., 2003). The VSOP Survey source monitoring program included $\sim$ 200 sources, and in each observing session only two scans, each of $\sim$ 1 minute duration, were obtained on each source at each frequency. The blazar monitoring program presented here obtained typically 6 scans of at least two minutes duration

in each observing session, which provided more accurate polarization measurements and more detailed information on source structure.

An important aspect of the ATCA blazar monitoring program, although not part of the original proposal, was that in addition to probing bi-monthly variability, it was possible to search for variability on time-scales shorter than a day. In this way, strong intraday variability (IDV) was discovered in PKS 1622−253. Comparing IDV and longer-term variability is important in order to understand and separate intrinsic variability from extrinsic effects such as interstellar scintillation. A detailed study of IDV sources is presented later in this thesis (Chapters 5 and 6).

This chapter presents the ATCA and LBA blazar monitoring observations. Analysis and interpretation of the observed radio variability is presented in Chapter 4.

3.2 The ATCA observations

3.2.1 The source sample

The core sample for the monitoring program presented here consists of all southern, compact, radio-loud blazars in the list of approved targets from the BeppoSAX 1st Announcement of Opportunity (AO1), to complement the northern sample observed at Medicina and Noto (Venturi et al., 2001). Some northern sources were also included in the ATCA program, in part for comparison of the measured flux densities between the different telescopes, but also because the ATCA provides polarization measurements which were not available with the single dish telescopes, as well as broader frequency coverage.

The 22 sources in the core sample are listed in Table 3.1, with coordinates, redshifts and optical identifications. There are no overall sample selection criteria as the sources are targets of various BeppoSAX projects. The sample includes a mixture of strong radio quasars and BL Lac objects at various redshifts; sources which are representative of the "blazar" phenomenon. All of these sources were observed in 12 or more epochs during the ATCA monitoring program.

Over the 3 year duration of the monitoring program, blazars from the BeppoSAX 2nd Announcement of Opportunity (AO2) target list were added to the sample, as well as radio-weak, high-energy peaked BL Lac objects (HBLs), plus some northern sources which were observed in only a few epochs with the ATCA. In total, approximately 60 sources have been observed as part of this program. The variability of the additional sources is not well-sampled in comparison to the core sample, and therefore only results for the core sample are presented here. Data on the other sources can be found in Appendix B.

3.2.2 The observations

As shown in Table 3.2, observations were carried out in sessions lasting 24 hours, approximately bi-monthly between May 1997 and August 1999. Another observation was

Table 3.1: Core sample for the ATCA blazar monitoring program. "ID" is classification from available literature. HBL = high-frequency peaked BL Lac object; LBL = low-frequency peaked BL Lac object; HPQ = high optically polarized quasar; LPQ = low optically polarized quasar; Q=quasar (optical polarization not available); RG = radio galaxy. Last column indicates sources also observed with the LBA.

Catalog name	(B1950)	RA (J2000)	Dec (J2000)	z	ID	LBA
PKS 0048−097		00:50:41.32	−09:29:05.2	...	LBL	•
PKS 0208−512		02:10:46.20	−51:01:01.9	0.999	HPQ	•
AO 0235+164		02:38:38.93	+16:36:59.3	0.940	LBL	
PKS 0420−014		04:23:15.80	−01:20:33.1	0.915	HPQ	•
3C 120	0430+052	04:33:11.10	+05:21:15.6	0.033	RG	
PKS 0528+134		05:30:56.42	+13:31:55.1	2.04	LPQ	
PKS 0736+017		07:39:18.01	+01:37:04.7	0.191	HPQ	
PKS 1144−379		11:47:01.37	−38:12:11.0	1.048	LBL	•
B2 1156+29	1156+295	11:59:31.83	+29:14:43.8	0.729	HPQ	
3C 279	1253-055	12:56:11.17	−05:47:21.5	0.538	HPQ	
PKS 1519−273		15:22:37.68	−27:30:10.8	...	LBL	•
PKS 1622−253		16:25:46.89	−25:27:38.3	0.786	Q	•
NRAO 530	1730-130	17:33:02.71	−13:04:49.5	0.902	LPQ	
PKS 1741−038		17:43:58.86	−03:50:04.6	1.054	HPQ	•
PKS 1933−400		19:37:16.22	−39:58:01.6	0.996	Q	•
PKS 2005−489		20:09:25.39	−48:49:53.7	0.071	HBL	•
PKS 2149−306		21:51:55.52	−30:27:53.7	2.345	Q	•
PKS 2155−304		21:58:52.07	−30:13:32.1	0.116	HBL	•
3C 446	2223-052	22:25:47.26	−04:57:01.4	1.404	HPQ	
CTA102	2230+114	22:32:36.41	+11:43:50.9	1.037	HPQ	
PKS 2243−123		22:46:18.23	−12:06:51.3	0.630	HPQ	•
3C454.3	2251+158	22:53:57.75	+16:08:53.6	0.859	HPQ	

scheduled in June 2000, extending the coverage over 3 years to give better measurements of variability in some of the slowly varying sources.

During an observing session, each source was observed at four frequencies, typically for between 2 and 5 minutes every two hours while it was above the 12° elevation limit of the ATCA. Observations were performed using 128 MHz bandwidth centred on frequencies of 1.384, 2.496, 4.800 and 8.640 GHz. These frequencies are recommended for continuum observations with the ATCA to minimise interference. The lower pair of frequencies was observed simultaneously, as was the higher pair of frequencies. Turret rotations at the ATCA may be performed only once per 15 minutes on average. The scheduling strategy therefore involved choosing a group of several sources occupying a small region of sky, for which the slewing time between each source would be short, typically $\lesssim$ 2 minutes. A short scan on each source was taken at the two lower frequencies, then the cycle was repeated at the two higher frequencies, before moving on to another group of sources. In this way, a large number of sources could be efficiently

Table 3.2: The ATCA blazar monitoring observations. Day numbering begins on January 1, 1997.

Start date	Epoch	MJD-50450	Duration (h)
1997-May-08	1997.35	128	24
1997-Jul-04	1997.51	185	24
1997-Sep-02	1997.67	245	27
1997-Oct-31	1997.83	304	28.5
1998-Jan-02	1998.01	367	24.5
1998-Jan-27	1998.07	392	11.5
1998-Mar-02	1998.17	426	25
1998-May-26	1998.40	511	24
1998-Jul-25	1998.56	571	27.5
1998-Sep-18	1998.72	626	24
1998-Oct-27	1998.82	665	24
1999-Feb-17	1999.13	778	24.5
1999-Apr-01	1999.25	821	25
1999-Aug-26	1999.65	968	23
2000-Jun-21	2000.47	1268	24

observed in 24 hours.

3.2.3 Data reduction

The MIRIAD software package (Sault et al., 1995) was used for data reduction. The steps involved in this procedure are outlined in Figure 3.1 and described in more detail below.

Editing

The observed datasets often contain some "bad data", which lead to measurement errors if not removed. The ATCA has an on-line flagging system which automatically flags data when antennas are not on source, or when the digital sampler levels are not within an acceptable range. However, it is usually necessary to remove some additional problem data. For the data presented here, the most common problems were caused by:

- **Interference:** this was particularly a problem at 2.5 GHz, largely due to intermittent interference from low Earth orbit satellites.[1] Solar interference, and interplanetary scintillation, can also be a problem for monitoring some sources

[1]The recommended frequency for 13 cm observations at the ATCA has now changed back to 2368 MHz, but this frequency was not usable for several years due to major interference in that part of the band.

Figure 3.1: Basic steps involved in calibrating the ATCA blazar monitoring data to obtain Stokes I, Q and U. MIRIAD task names appear in brackets. Note that this procedure is designed to give accurate daily average measurements and is not suitable for studies of intraday variability. See Section 3.2.3 for details.

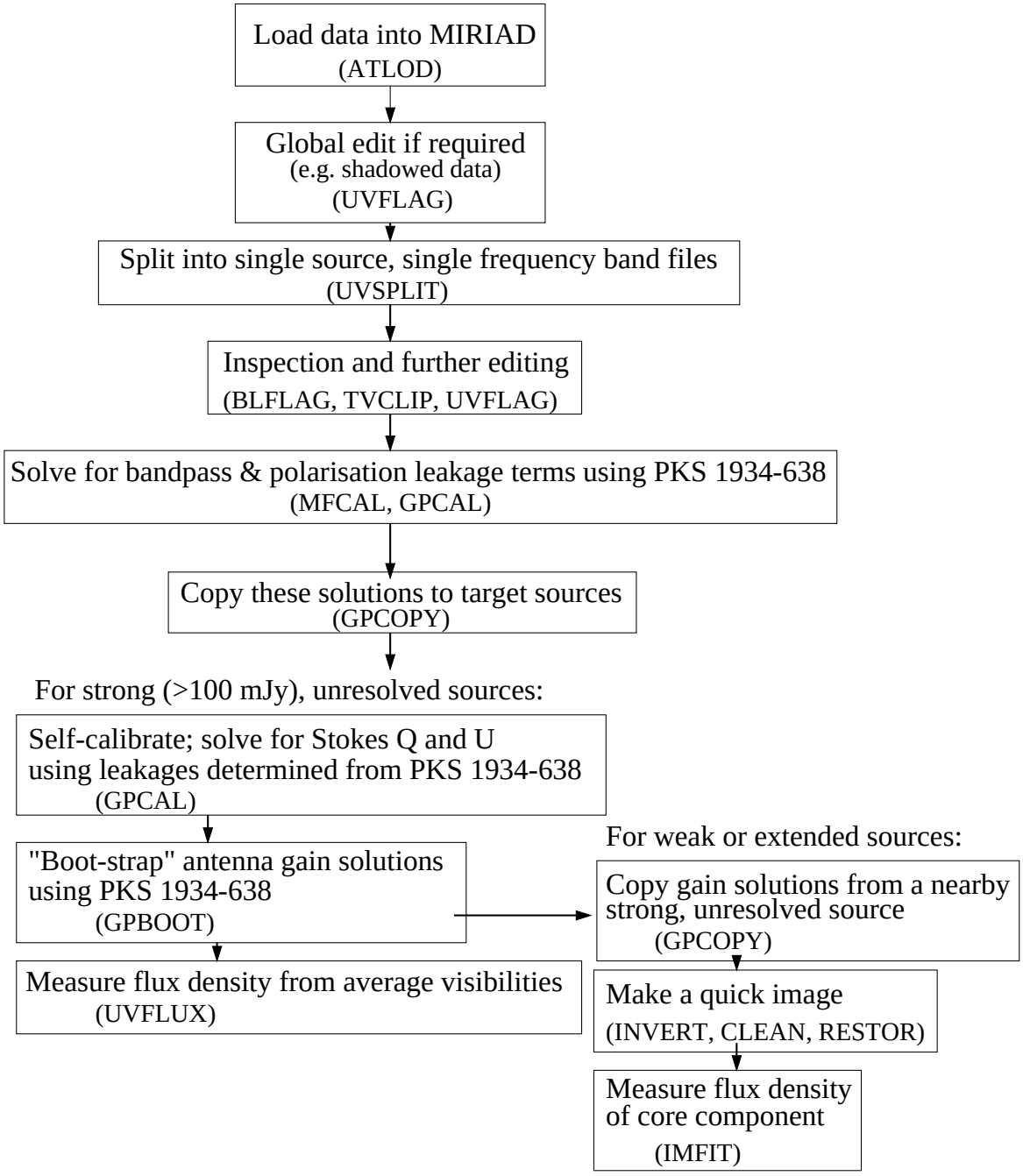

at particular times of the year when they are close to the sun. This effect is most significant at the two lower frequencies.

- **Weather:** while this is more of a consideration for higher frequency observations, heavy rain and storms result in highly variable system temperatures, and attenuation of signal, at cm-wavelengths. Bad weather can thus lead to incorrect flux density measurements. The severity of this problem increases toward higher frequencies.

- **Antenna tracking problems:** occasionally when an antenna was off source, data were not flagged on-line. These problems were usually due to Antenna Control Computer (ACC) errors or drive failures.

- **Shadowing:** only occurs for some ATCA configurations. On very short baselines and when antennas are at low elevation, one antenna's aperture may be blocked or "shadowed" by another antenna, reducing the visibility amplitude on all baselines to that antenna.

For the data presented here, three MIRIAD tasks were used to remove bad data. UVFLAG is a non-interactive task which was used to automatically remove data affected by shadowing, or where some other known problem occurred. TVCLIP was used non-interactively to remove most outlying data caused by interference, and finally, all data were inspected by eye using BLFLAG, an interactive baseline editor, which was used to remove remaining bad data, e.g. where amplitudes on baselines to one antenna were significantly reduced or showed anomalous scatter. Intraday variable (IDV) data are not flagged in this process because IDV affects all baselines the same way.

Calibration

The flow-chart in Figure 3.1 illustrates the reduction process used to obtain average flux density and linear polarization measurements for all sources in each observing session. All sources in the core sample are strong and mostly unresolved with the ATCA. In fact most of these sources are listed in the ATCA or Very Large Array (VLA) calibrator catalogs as secondary calibrators, and the calibration procedure used is the path recommended in the MIRIAD Users Guide for secondary calibration.

The overall flux density scale is determined in each session from high-elevation observations of the ATCA primary calibrator, PKS 1934−638, for which the flux density is known (Reynolds, 1994), and has been found to be non-variable. PKS 1934−638 was also used to determine the bandpass correction, as well as the instrumental polarization (see Section 2.3.3), at each frequency and for each session. Bandpass and polarization leakage terms are assumed to be constant over the 24 hour observing sessions, an assumption supported by observations which show that the bandpass solutions from observations months apart are virtually identical, and similarly, polarization leakages derived from observations several months apart are often the same within $\sim 0.1\%$.

For compact sources stronger than ~ 100 mJy, which includes all sources in the core sample, calibration of the complex antenna gains was performed using a point source model. Task GPCAL in MIRIAD was used for this purpose. Phase variations can be quite rapid, especially at the higher frequencies, depending mainly on tropospheric conditions, and short solution intervals (usually equal to the 10-second integration cycle of the correlator) were chosen to avoid loss of signal due to "phase wrapping" when vector averaging. GPCAL, unless given an *a priori* source flux density, attempts to set the gain amplitudes so that the average is 1. The resultant amplitude gains are then scaled by a constant factor derived from a near-transit observation of the primary calibrator PKS 1934−638, at an elevation of $\sim 55°$. The scaling factor can be up to a few percent, depending on the initial set-up of the observation, but should be the same for all sources at each frequency. Inspection of these scaling factors provides a useful check on (i) whether any bad data are still present, and (ii) whether a point-source model is reasonable. Data where the scaling factor was discrepant were further examined and edited where necessary, or imaged in the cases where extended emission was evident.

The above method was used to give measurements of the average flux density and linear polarization for each source in each observing session, as accurately as possible. Using GPCAL in this way is, however, a problem for IDV sources, as the antenna gains will be adjusted to remove the IDV! To search for IDV, phase-only self-calibration was performed using task SELFCAL in MIRIAD, after first applying the bandpass, leakages and a time-independent gain correction from PKS 1934−638.

In some sessions, weak or significantly extended sources were observed, in which case the gain solutions were copied from a nearby, compact source. The data were then imaged to measure flux density, as indicated in Figure 3.1.

Measuring flux densities

The MIRIAD task UVFLUX was used to obtain a mean visibility value, averaged over all baselines, for Stokes I, Q and U in each dataset. For strong, point-like sources, provided phase self-calibration has worked, then the vector-averaged, real part of Stokes I is identical, or very close to, the scalar-averaged amplitude of Stokes I. The amplitude scalar average is not affected by phase errors, whereas the real part will decorrelate if phase errors are present. For Stokes Q and U, which have lower signal-to-noise ratios, it is necessary to take the vector-averaged real parts, as the noise adds significantly in the amplitude; good phase calibration is therefore important. The real parts of Stokes Q and U were also converted to linearly polarized flux density, $p = \sqrt{Q^2 + U^2}$, and position angle $\psi = 1/2 \arctan(U/Q)$, since p, ψ and Q, U are equivalent representations (see Section 2.3.3).

Estimation of errors

For long-term variability monitoring, it is important to estimate the errors in comparing flux densities measured in different observing sessions. For studies of intra-day

variability, the major concern is how reliably the flux density can be measured from single scans over the course of the observing session.

There are four main contributions to the error in measuring Stokes I, Q and U:
(i) thermal or receiver noise;
(ii) confusion from unrelated sources, or extended structure in the target source itself, the contribution of which may vary slightly from epoch to epoch due to different sampling of the (u, v) plane, which will occur for different array configurations and for scans taken at slightly different hour angles. The varying response of the array to extended structure is a particularly important consideration for IDV observations. The amount of flux density in extended components has been estimated for each source from the observed closure phases, using Equation 2.11;
(iii) calibration errors: errors in the antenna gain solutions contribute errors proportional to the flux density;
(iv) the long-term flux density stability of the ATCA primary calibrator, PKS 1934−638.

Here it is assumed that PKS 1934−638 did not vary over the 3 years of the present observations, a reasonable assumption from the long-term flux density monitoring program for VSOP sources, which found that a number of sources did not vary with respect to PKS 1934−638 (Tingay et al., 2003). For the reduction procedure described above, the errors are estimated from the root-mean-square (rms) scatter of the data about the mean, and from the rms scatter of the antenna gain solutions. Since all sources in the core sample are self-calibrated assuming a point-source model, any significant deviation of the source structure from this model will result in the rms scatter of the data being significantly larger than the theoretical scatter due to thermal noise. Unsubtracted structure may also result in spurious variations in antenna gain solutions. The overall contribution of extended structure is approximately the same in each epoch, as scans are generally made at approximately the same hour angles in different sessions. However, as the shortest baseline lengths are different for the various ATCA configurations used, data on the very short baselines are discarded to reduce the response to diffuse, extended emission. Taking all sources of error into account, the rms scatter of the antenna gain amplitude solutions is used to estimate the total proportional error, and the rms scatter of the calibrated data is a measure of the error due to noise and confusion.

The total error in a flux density measurement, σ_I, is then estimated as

$$\sigma_I = \sqrt{\epsilon_I^2 + (\sigma_g I)^2}, \tag{3.1}$$

where I is the measured flux density from Stokes I visibilities; $\epsilon_I = rms(I)/\sqrt{N_{\rm corrs}}$ is the error-in-the-mean of the calibrated Stokes I visibilities—$rms(I)$ is the rms scatter of the real and imaginary parts of the visibilities around their mean value, and $N_{\rm corrs}$ is the number of correlations used in forming each mean; and σ_g is the standard deviation of amplitude gain solutions for all antennas, both X and Y polarizations. The values obtained for σ_I in this way are typically $\sim 1 - 2\%$ rms at all frequencies, for sources which do not show significant extended emission.

Using σ_g in this way as an estimate of the proportional errors may in fact give a slight overestimate of the errors. However, ultimately, the flux density scale for comparison

of measurements in different epochs is set from only a single scan on PKS 1934−638, so it is important to estimate how variable the amplitudes may be over the course of the observation. The values obtained for σ_g are comparable with other error estimates, for example, long-term modulation indices for non-variable sources, presented later in Chapter 5. Importantly, the variance of the gain solutions seems to be a good indicator of problem data; for example, in very bad weather conditions, the amplitudes are much more variable than usual, particularly at 8.6 GHz, and the flux density measurements have much larger associated errors. The weather was particularly bad for the observations of 1999 April 1.

A method similar to the above is used to estimate the errors in Stokes Q and U, and hence p, the linearly polarized flux density; in most cases, $\sigma_Q \approx \sigma_U \approx \sigma_p$. Errors in leakage terms and the relative amplitudes of X and Y gains also contribute to errors in the measurement of Stokes Q and U, and such errors are proportional to the *total* flux density. The leakage solutions are estimated to be accurate to within 0.1%. Errors in p are then estimated as

$$\sigma_p = \sqrt{\epsilon_p^2 + (\sigma_g p)^2 + (0.001I)^2}, \tag{3.2}$$

where ϵ_p is the standard deviation in Stokes Q or U, whichever is larger, and the other parameters are as for Equation 3.1. The error in polarization position angle, ψ, is estimated as $\sigma_\psi = 0.5\sigma_p/p$ radians (e.g. Rayner, 2000).

Search for intraday variability

In each observing session, each source was observed in approximately 6 scans at each frequency, which allows intraday variability (IDV) to be investigated. There has recently been much debate over the origin of radio IDV (see Section 1.3.6) observed in some compact, flat-spectrum radio sources. Two sources in the core sample had been found to exhibit significant IDV from the ATCA IDV Survey of Kedziora-Chudczer et al. (2001b): PKS 1519−273 and PKS 1144−379. Rapid variability has also been observed in AO 0235+164 (Kraus et al., 1999a).

For the calibration strategy shown in Figure 3.1, any IDV present will be "removed" by time-dependent self-calibration using task GPCAL, since the complex gains are adjusted assuming a constant flux density, although IDV will result in increased antenna gain variations and hence larger error bars. In order to search for intraday variability within each dataset, a different calibration strategy was adopted. Firstly, as above, global solutions for antenna gain, bandpass and leakage were applied using PKS 1934−638. Phase-only self-calibration was then applied, using a point source model. The real parts of Stokes I, Q and U for each epoch were then plotted, averaging over all baselines and over 1 minute in time for Stokes I, and across the scan length for the weaker Stokes Q and U signals. The modulation indices, $\mu_I = \sigma_I/\bar{I}$, $\mu_Q = \sigma_Q/\bar{Q}$, and $\mu_U = \sigma_U/\bar{U}$ were then calculated for the data within each epoch, for each source and each frequency. In the case of low signal-to-noise in Stokes Q and U, the fractional variability may appear to be very large simply due to measurement

uncertainties, and therefore σ_Q and σ_U were used in place of the modulation index as an additional statistic for polarization variability.

For sources with significant ($> 4\%$) extended structure or confusion indicated by the closure phases, Stokes I was ignored, because of the large variation in visibilities due to the varying response of the ATCA to structure over the course of a day. This is mainly a problem at 1.4 GHz because of significant confusion. The mean $\bar{\mu}$ and standard deviation σ_μ of the modulation index for each epoch, frequency and Stokes parameter were calculated, and data for sources where $\mu > \bar{\mu} + \sigma_\mu$ were further inspected. Generally, it is possible to distinguish between real IDV and variation of visibilities due to structure by inspecting data on all 15 baselines, because an IDV pattern is the same on all ATCA baselines, whereas structure is not.

3.2.4 Results

Long term variability and average properties

Flux density measurements, averaged over each observing session, for all sources in the core sample are presented in Appendix A. For each source, two pages of plots are presented. The first window shows the total flux density (top panel), linearly polarized flux density (middle panel) and position angle of the electric vector of linear polarization (EVPA; third panel) at each of the four observed frequencies. Error bars, calculated as described in Section 3.2.3, are shown. Total flux density errors are typically 1–2% at all frequencies, but can be higher due to unsubtracted confusion or source structure, or bad weather. To avoid spurious, large position angle variations in the case of very weak signals in Stokes Q and U, polarization position angle is only plotted when the polarized flux density exceeds a 3σ detection, where σ is the estimated standard error in p as defined above in Section 3.2.3. The window on the bottom of the first page of plots for each source shows the total flux density spectral evolution, from every second epoch. On the second page of plots, an alternative representation of the linear polarization is shown: the path of the $\mathbf{p}$ vector in the (Q, U) plane is plotted for each frequency. This representation is further discussed in Section 4.2.4. Also shown, in the panel below the (Q, U) diagrams, is the polarized flux density spectral evolution, which sometimes shows quite similar behaviour to the total flux density but is often somewhat more complicated. Analysis of these light curves and interpretation of source properties is presented in Chapter 4.

While all observed sources show significant variability at most frequencies, the mean flux density and spectral index of a source are representative quantities which are often correlated with other properties. Table 3.3 shows the average flux density and two-point spectral indices for sources in the core sample. Also shown is the estimated fraction of flux density outside of the unresolved core for each source, calculated from the closure phases using Equation 2.11, which is typically larger at the lower frequencies, as expected due to confusion. At 8.6 GHz the fractional extended flux is $\lesssim 2\%$ for all sources in the core sample.

Table 3.4 shows the mean linearly polarized flux density, and fractional linear polar-

Table 3.3: Mean radio properties of the ATCA core sample, at 1.4, 2.5, 4.8 and 8.6 GHz. α is the mean two-point spectral index, where $S_\nu \propto \nu^\alpha$. $S_{\rm ext}/S_{\rm tot}$ is the percentage of extended emission or confusion estimated from the closure phases. See Section 3.2.4 for details.

IAU name	Flux density (Jy)				α		$S_{\rm ext}/S_{\rm tot}$ (%)			
(B1950)	1.4	2.5	4.8	8.6	$\alpha_{1.4}^{4.8}$	$\alpha_{4.8}^{8.6}$	1.4	2.5	4.8	8.6
0048−097	0.82	0.99	1.26	1.40	0.34	0.16	8.4	4.4	1.6	1.1
0208−512	3.62	3.28	3.00	2.81	−0.15	−0.13	4.9	3.6	2.5	1.6
0235+164	0.82	1.02	1.58	2.13	0.47	0.51	5.1	2.3	0.9	0.9
0420−014	1.98	2.18	2.74	3.19	0.26	0.25	2.2	1.1	0.6	0.8
0430+052	3.63	3.88	4.32	4.36	0.14	0.01	5.8	4.3	2.3	1.5
0528+134	2.33	2.98	3.40	3.50	0.30	0.05	1.8	1.4	0.6	0.9
0736+017	2.04	1.74	1.62	1.62	−0.19	−0.01	2.8	1.9	1.0	1.0
1144−379	1.40	1.56	2.03	2.58	0.31	0.40	13.0	5.8	2.7	1.4
1156+295	1.61	1.40	1.50	1.76	−0.10	0.18	1.5	1.0	1.0	1.7
1253−055	8.70	10.46	16.44	23.77	0.51	0.63	7.0	4.0	2.3	1.2
1519−273	1.03	1.36	1.71	1.68	0.41	−0.03	3.4	1.2	0.5	0.9
1622−253	1.80	1.76	1.98	2.30	0.05	0.24	4.1	2.7	1.5	1.2
1730−130	5.37	5.49	6.19	6.10	0.09	−0.06	2.7	2.1	1.3	1.1
1741−038	1.80	3.18	4.60	5.07	0.76	0.16	2.4	0.7	0.4	0.8
1933−400	0.96	0.92	0.95	0.90	−0.01	−0.09	5.6	2.8	1.3	1.5
2005−489	1.27	1.29	1.29	1.20	0.00	−0.12	3.8	1.5	0.7	1.0
2149−306	1.24	1.63	1.81	1.62	0.30	−0.20	4.8	2.4	1.6	1.2
2155−304	0.39	0.40	0.41	0.41	0.04	−0.02	8.2	4.6	2.0	1.9
2223−052	5.95	4.76	4.60	4.95	−0.21	0.10	7.3	3.5	0.6	0.8
2230+114	6.88	5.63	4.85	4.68	−0.28	−0.07	0.4	0.6	0.9	1.3
2243−123	1.87	1.97	2.10	2.25	0.09	0.11	1.5	1.1	0.8	0.9
2251+158	13.84	13.00	12.83	11.41	−0.06	−0.20	4.0	3.9	2.3	1.7

Table 3.4: Mean linear polarization for the core sample. p=linearly polarized flux density, m_p=fractional linear polarization.

IAU name	p (mJy)				m_p (%)			
(B1950)	1.4	2.5	4.8	8.6	1.4	2.5	4.8	8.6
0048-097	21	25	39	70	2.5	2.5	3.1	4.8
0208-512	67	52	47	45	1.9	1.6	1.6	1.6
0235+164	6	10	23	26	0.7	1.0	1.3	1.1
0420-014	41	48	46	59	2.0	2.2	1.7	1.8
0430+052	99	164	122	146	2.7	4.2	2.9	3.4
0528+134	6	15	53	55	0.3	0.5	1.5	1.6
0736+017	176	145	114	83	8.6	8.3	7.1	5.3
1144-379	27	33	38	58	1.9	2.1	1.9	2.3
1156+295	44	24	25	33	2.7	1.8	1.9	2.1
1253-055	223	373	724	552	2.6	3.5	4.5	2.3
1519-273	22	30	47	56	2.2	2.3	2.8	3.3
1622-253	21	16	20	36	1.2	1.0	1.1	1.5
1730-130	152	158	183	233	2.8	2.9	3.1	3.8
1741-038	9	22	44	81	0.5	0.7	1.0	1.6
1933-400	30	28	32	16	3.1	3.0	3.4	1.8
2005-489	41	52	48	37	3.2	3.9	3.7	3.0
2149-306	23	27	90	106	1.8	1.7	4.9	6.5
2155-304	14	14	12	11	3.6	3.5	2.8	2.7
2223-052	321	241	215	160	5.4	5.0	4.7	3.3
2230+114	127	126	124	118	1.9	2.2	2.6	2.6
2243-123	17	21	21	33	0.9	1.1	1.0	1.5
2251+158	856	736	408	194	6.2	5.6	3.2	1.7

ization, for all sources in the core sample. Although the polarization is quite variable, the table shows that the mean fractional polarization is always $< 10\%$, and for most sources is between 1 and 5%.

Intraday variability

Although it was not an aim of the original proposal, the ATCA blazar monitoring program allowed searches for variability on time-scales shorter than a day. Few extragalactic sources are known to vary on time-scales shorter than ~ 12 hours. Previous studies of short-term variability (e.g. Heeschen et al., 1987) have found that variability on time-scales of several days is more common. Since the present monitoring program observed sources over only one day, every two months, variability occuring on time-scales of several days would be missed. Nevertheless, strong IDV was discovered in one new source, and observed in two sources which had shown strong IDV in the ATCA IDV Survey (Kedziora-Chudczer et al., 2001b).

Strong intra-day variability was discovered in PKS 1622−253. Interestingly, this

source had not met the selection criteria to be included in the ATCA IDV Survey (Kedziora-Chudczer et al., 2001b). The IDV Survey sources were chosen to meet the "compactness" condition that the ratio of the flux density measured with the Parkes-Tidbinbilla Interferometer (PTI) to the total flux density measured with the Parkes single dish, at 2.3 GHz, was larger than 0.9. However, for PKS 1622−253 this ratio was only 0.64 (Duncan et al., 1993). Such a low visibility ratio could be largely due to significant, arcsecond-scale extended emission, which is indicated in ATCA and LBA data (see Section 3.3.4). Figure 3.2 shows an ATCA image of the source at 4.8 GHz. The measured PTI to total flux density ratio may also be reduced due to source variability, if the flux density was lower at the time of the PTI measurement than at the time of the total flux density measurement, since the single dish and PTI flux density measurements were not made simultaneously.

Despite its significant arcsecond scale structure, PKS 1622−253 showed large-amplitude IDV during some epochs of the blazar monitoring observations, particularly at 8.6 GHz, as shown in Figures 3.3 and 3.4. Figure 3.3 shows the amplitudes of observed visibilities over the course of a day on all baselines, plotted as a function of distance in the (u, v) plane. The vertical displacement between different scans indicates a change in flux density which is not due to source structure. The lower panel in Figure 3.3 shows an average of the visibilities with (u, v) range greater than 50 Mλ, to remove most of the effect of extended structure. For data presented later in Chapter 5, the arcsecond scale structure of PKS 1622−253 has been modelled, and the components outside the unresolved "core" have been subtracted from the visibilities. However, the presence or absence of extended structure makes little difference to the large-amplitude intraday variations observed for this source.

Figure 3.4 shows IDV in total and polarized flux density, and position angle of the E vector of linear polarization, for PKS 1622−253, measured in an observation starting on October 31, 1997. This figure shows that the variations in polarized flux density are not directly correlated with the variations in total intensity. For comparison, data over the same time range for the non-IDV source NRAO 530 are also shown. From a comparison of the average flux densities in Figures 3.3 and 3.4, and the long-term monitoring of PKS 1622−253 (see Figure A.12), it is clear that the mean flux density of this source changes dramatically on longer time-scales.

Strong IDV was also observed in PKS 1519−273 and PKS 1144−379, both of which had been found to show strong IDV in the ATCA IDV Survey (Kedziora-Chudczer, 1998; Kedziora-Chudczer et al., 2001b). Examples of the IDV observed in the present project are shown in Figure 3.5. PKS 1519−273 stands out as the source which consistently shows the largest amplitude IDV in both total and polarized flux density, particularly at 2.5 and 4.8 GHz. PKS 1144−379 showed strong IDV in some epochs of the ATCA blazar monitoring. This source lies in a heavily confused field which makes analysis of IDV difficult, particularly at the lower frequencies. Similarly to PKS 1622−253, PKS 1144−379 shows large outbursts on longer time-scales (see Figure A.8). The mean flux density at 8.6 GHz almost doubled in 1998 between January and May, and decreased by the same amount between May and September of the same year. For PKS 1519−273, however, the amplitude of long-term variability is not sig-

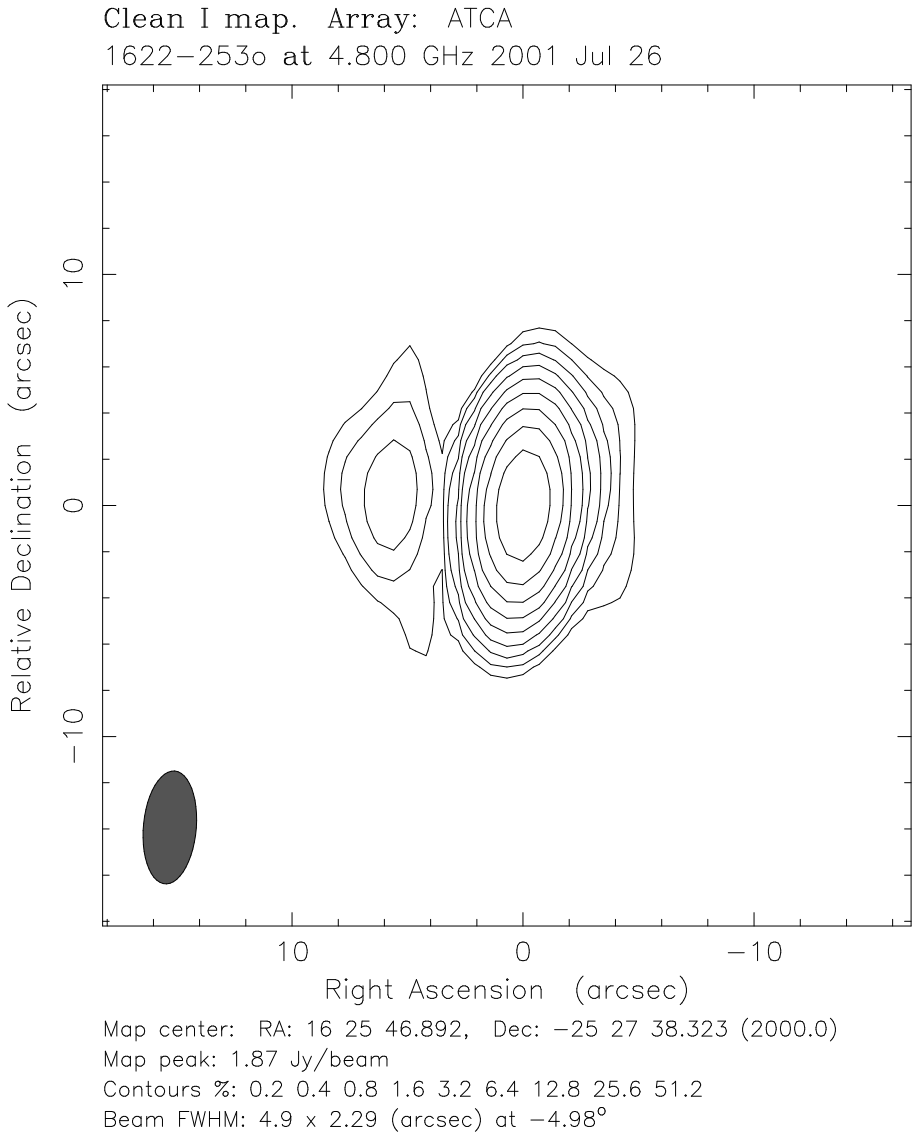

Figure 3.2: ATCA image of PKS 1622−253 at 4.8 GHz, from an observation in July 2001.

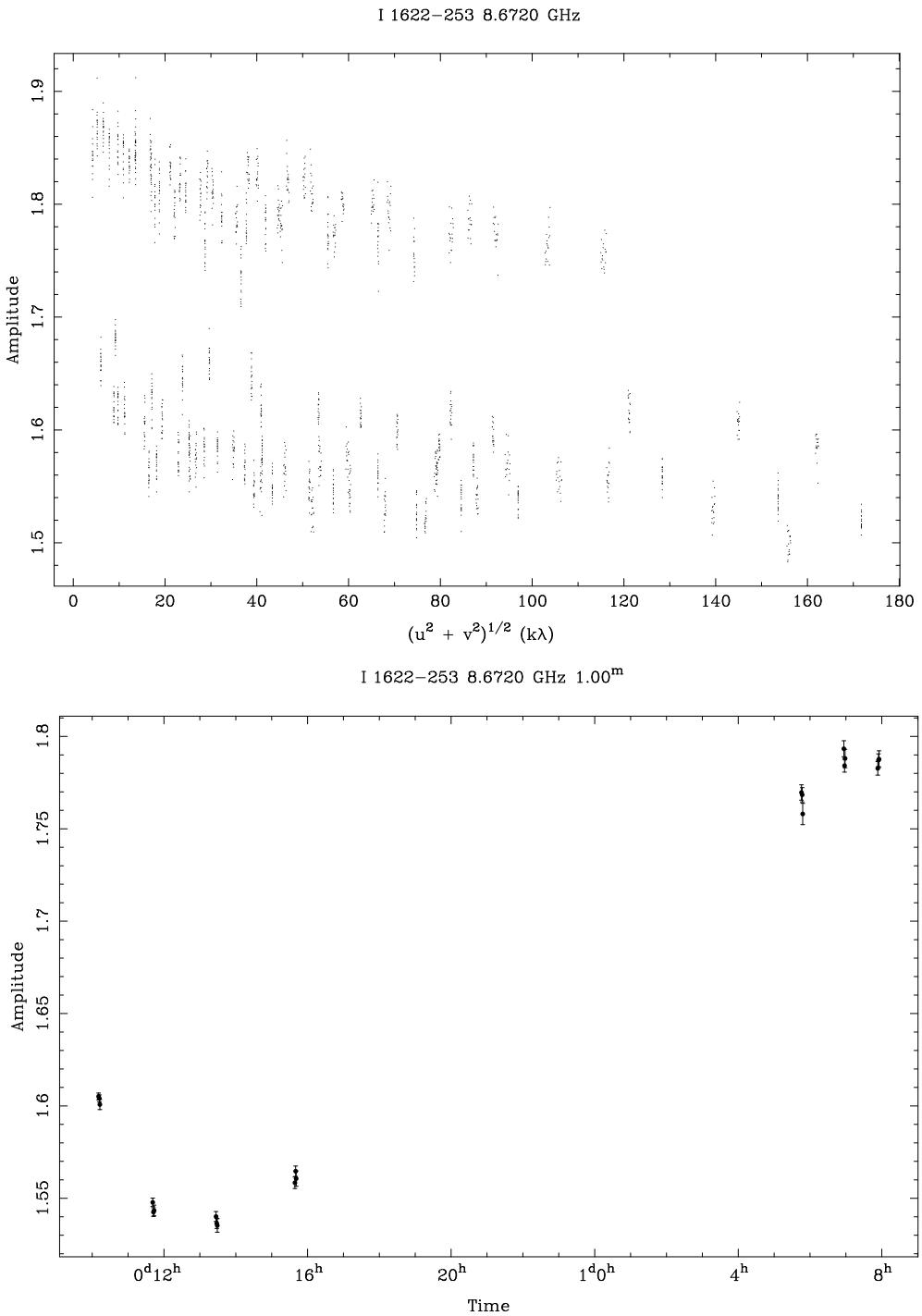

Figure 3.3: Upper panel shows Stokes I visibility amplitudes as a function of distance in the (u, v) plane for PKS 1622−253, from an observation over 24 hours in July 1997. The vertical displacement indicates a change in flux density between scans observed at different times, as shown in the lower panel, which shows all baselines averaged together over 1 minute, plotted as a function of time. Visibilities in this plot are restricted to those with (u, v) range greater than $50\,\mathrm{M}\lambda$ to remove most of the response to extended structure, although this makes no significant difference to the observed variation. The vertical scales are in Jy.

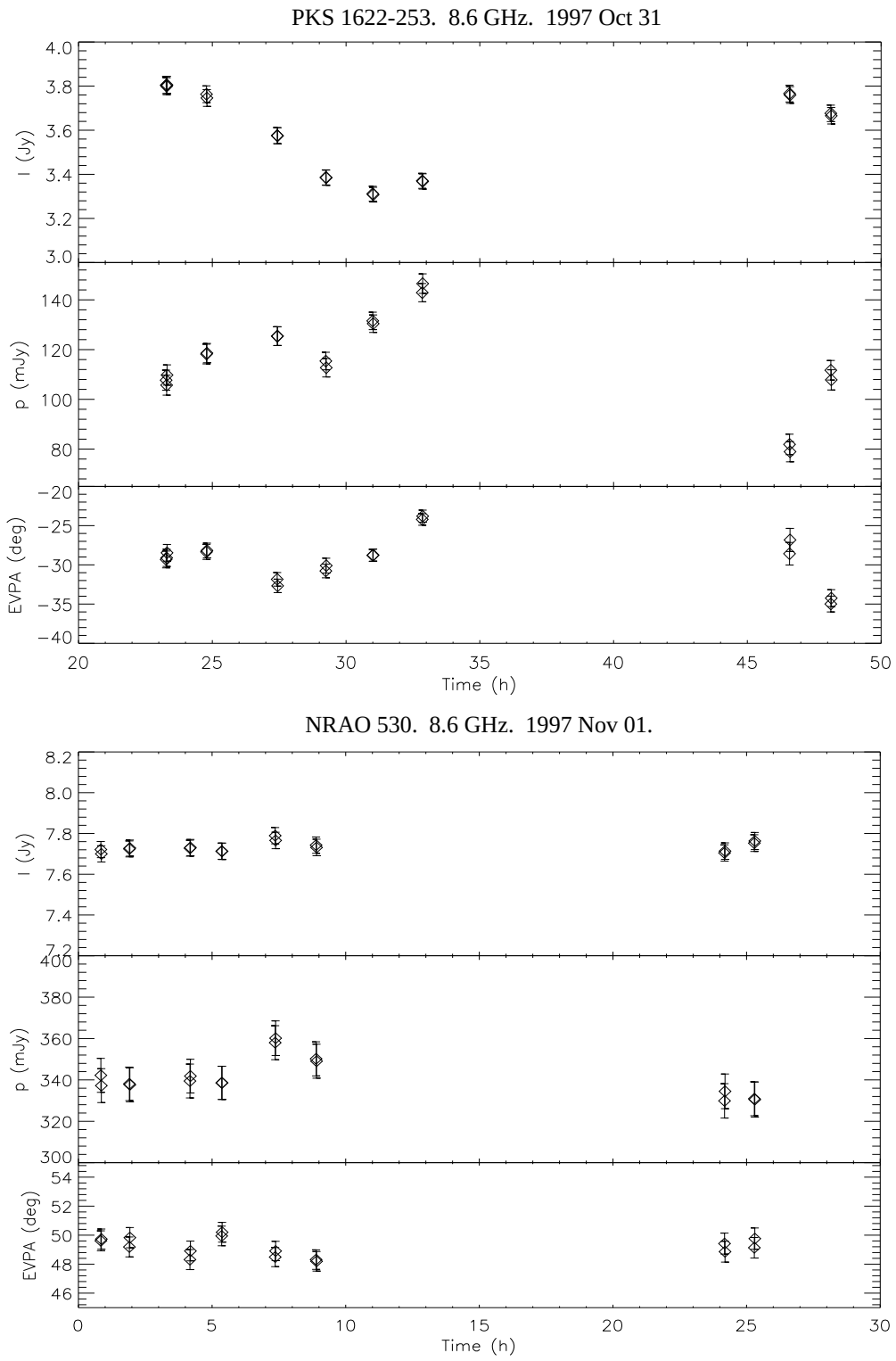

Figure 3.4: Total flux density (I), linear polarization (p) and electric vector position angle (EVPA) of linear polarization for PKS 1622−253 and NRAO 530 (B1730−130), measured at 8.6 GHz during the observation starting on 1997 Oct 31. Data are averaged over all baselines, and plotted with 1-minute time averaging.

nificantly different to the amplitude of IDV, which can be seen more clearly from the data presented in Chapter 5.

The radio variability of the three "extreme" IDV sources, PKS 1144−379, PKS 1519−273 and PKS 1622−253, and other selected sources, is further discussed in Chapter 4, along with the general long-term variability behaviour of all sources in the core sample.

3.3 The VLBI Observations

3.3.1 Source selection

A sub-sample of sources for monitoring with the LBA was selected from the larger ATCA sample (see Table 3.1). The selected sources all had $\delta < 0^\circ$ and a strong (> 100 mJy) core detected in previous VLBI observations. These selection criteria gave 12 sources suitable for monitoring with the sensitivity of the LBA. These 12 sources are indicated in Table 3.1. In addition, two sources, PKS 0537−441 and PKS 1921−293, which are also blazars, were observed in one or two short scans during each epoch for fringe-finding and calibration. From previous observations, these two sources were known to have strong VLBI "cores", and thought to have little extended structure between the arcsecond scales measured with the ATCA, and the shortest LBA baselines.

3.3.2 The observations

The full sample of 12 blazars was observed at both 2.3 and 8.4 GHz, in five observing sessions between June 1997 and November 1998. In March and September 1999, only the four southernmost sources were observed, using the Australian telescopes in conjunction with the 26-m antenna at Hartebeesthoek in South Africa, to obtain higher angular resolution observations for these sources. Table 3.5 lists the length of each observing session, telescopes involved and number of sources observed with the LBA in each session. For three other sources in the sample, a single epoch of higher resolution observations was obtained with the VLBA. The results of these observations are presented in Section 3.3.5.

The observing setup differed slightly from session to session. In three sessions, right-hand circularly polarized (RCP) data were recorded in two contiguous, 16 MHz bands, utilising the maximum data recording rate of $128\,\mathrm{Mb\,s^{-1}}$, while in another three sessions, only one 16 MHz band was recorded with a data rate of $64\,\mathrm{Mb\,s^{-1}}$. In the first observing session, both left-hand and right-hand circularly polarized data were recorded, each over the same 16 MHz band, except at Hobart where the receiver only allows measurement of RCP radiation. At the time of writing, polarimetric calibration for the LBA is under development and no polarimetry was attempted in the observations presented here. While recording two 16 MHz bands at adjacent frequencies allows some consistency checks, the $\sqrt{2}$ improvement in signal to noise obtained by doubling the bandwidth was not important, as systematic errors are much larger than

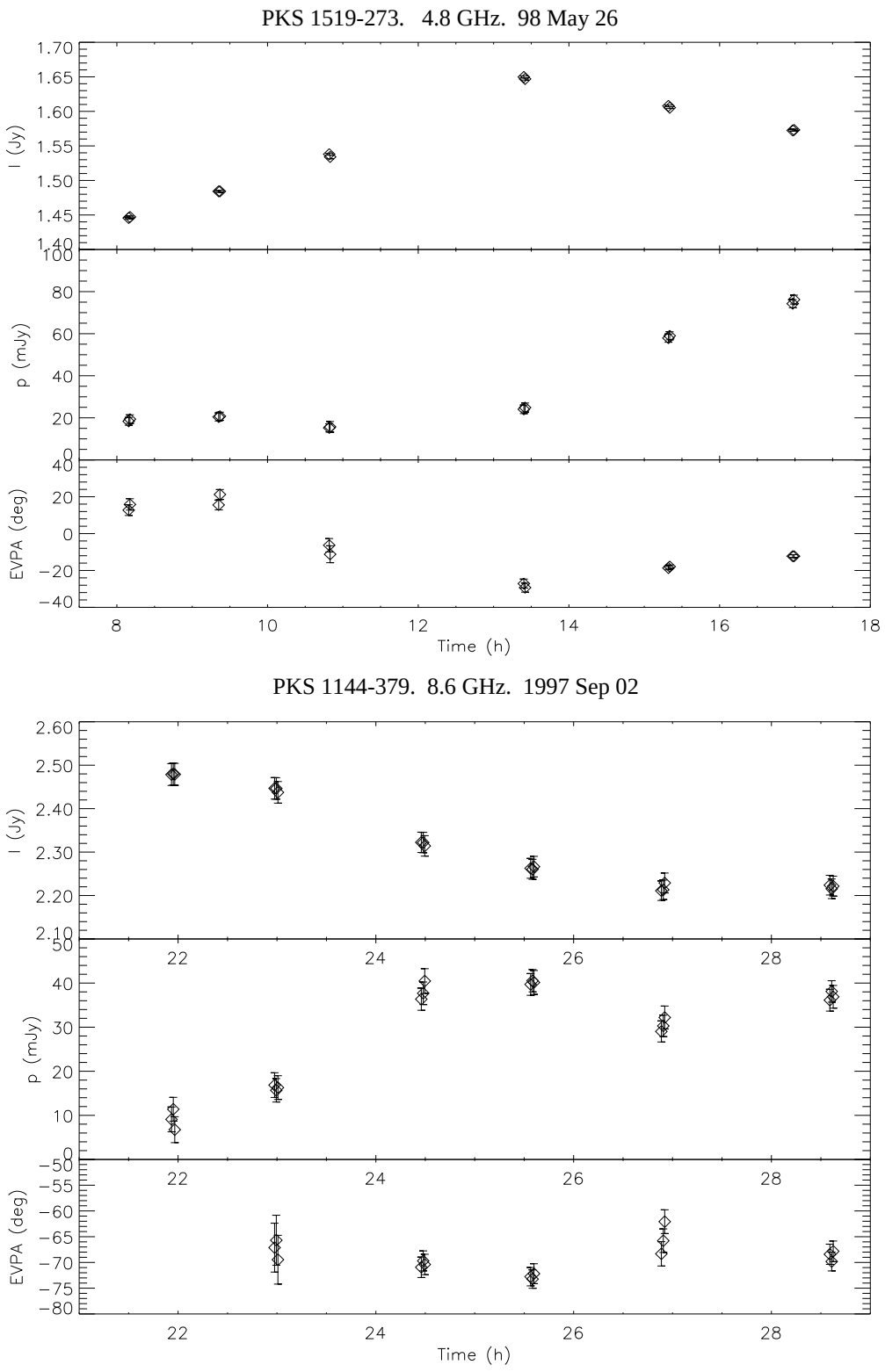

Figure 3.5: Examples of intraday variability in sources observed with the ATCA. Plotted are the total (Stokes I) and linearly polarized (p) flux density, and position angle of the electric vector of linear polarization (EVPA), each averaged over 1 minute intervals. Upper panel: PKS 1519−273 at 4.8 GHz. Lower panel: PKS 1144−379 at 8.6 GHz.

Table 3.5: LBA observations. PKS=Parkes, CAT=ATCA tied array, MOP=Mopra, HOB=Hobart, Tid=Tidbinbilla (either DSS43 or DSS45), CED=Ceduna, HAR=Hartebeesthoek. ∘ = antenna only available for part of experiment. ∗ = 100% of data lost.

Epoch	Duration	Stations involved							$N_{\rm sources}$
	of obs (h)	CAT	MOP	PKS	TID	HOB	CED	HAR	target+cal
1997.45	48	•	•	•		•			12+2
1997.93	56	•	•	•	∘	•			12+2
1998.21	48	•	•	•		•			12+2
1998.55	48	•		•	∘	•			12+2
1998.85	48	•	•	•		•			12+2
1999.19	48	•	•	•	∘	∗	•	•	4+1
1999.71	36	•	•	•	∗	•		•	4+2

the thermal noise for all observed sources.

In most observing sessions, each source was typically observed for ~ 5 scans each of ~ 20 minutes duration. For the two observing sessions in 1999, fewer sources were observed and hence each source was observed for longer. The observing schedules for these two sessions were designed to obtain maximum coverage of all sources during their period of common visibility with the LBA and the antenna in South Africa. Typically, even far-southern sources can only be observed with Hartebeesthoek and the LBA for a few hours each day, due to the curvature of the Earth! As the Hartebeesthoek antenna has an equatorial mount, it is also limited to an hour angle range of ± 6.5 hours. Figure 3.6 shows typical (u, v) coverage obtained for sources at various declinations.

3.3.3 Data analysis

Following the observations, correlation, fringe-fitting and calibration were performed, as described in Section 2.4.3. The accuracy of the LBA calibration, for the data presented here, is in practise always limited by system stability rather than signal-to-noise. Problems at one or more antennas, resulting in either loss of data, or a reduction in data quality, occurred in most observing sessions.

Problems encountered

- Pointing problems: occasionally, severe pointing errors occurred at one of the antennas, in which case the data on all baselines to that antenna had to be discarded.

- Wind-stows: antennas being stowed due to high wind is another problem which causes data to be lost; the Mopra site is particularly prone to high winds, and often there were some gaps in observations due to wind-stows.

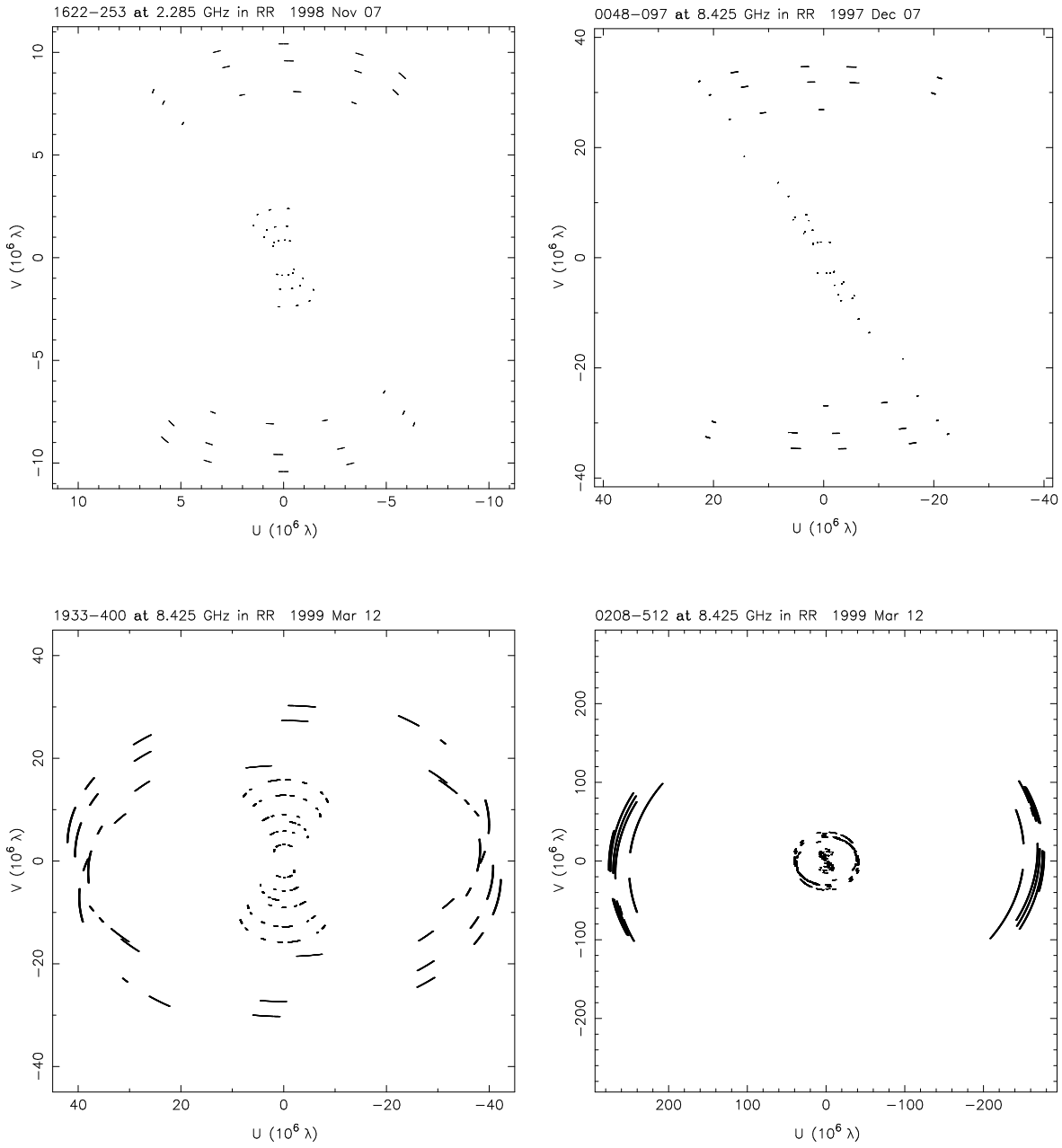

Figure 3.6: Typical (u, v) coverage obtained with the LBA for sources at various declinations. Upper panels show (u, v) coverage for observations with participating stations Parkes, Mopra, Narrabri and Hobart, at 2.3 GHz (upper left) and 8.4 GHz including one scan with Tid (upper right). Lower panels are for 8.4 GHz observations in 1999 March. The participating stations were Parkes, Mopra, Narrabri, Tid and Ceduna and Hart (Hobart data were unusable due to a pointing problem). Baselines to Hart are shown only in the lower right-hand plot.

- Loss of "coherence" or phase stability: the local oscillators at each station are locked to a Hydrogen maser frequency standard. Sometimes, however, a problem occurs in the system, resulting in poor coherence at a particular station. This causes degradation of data due to poorly behaved phases, or loss of data in the case of total loss of coherence.

- Recording of system temperature, T_s: problems with T_s measurements usually increased measurement uncertainties but did not cause loss of data. There were some periods, or occasionally entire observing sessions, where no T_s was recorded at a particular antenna, or erroneous values were recorded, meaning that *a priori* T_s values had to be assumed. Based on a comparison of data calibrated using measured T_s values with data calibrated using a constant value for T_s, amplitude errors are typically $\lesssim 10\%$ in good observing conditions where measured T_s is not available. In bad weather conditions T_s variations may be much larger, sometimes requiring data to be discarded. In fair weather, most of the variation in T_s occurs towards low elevations, which can be compensated for if an antenna "tipping curve" has been derived. *A priori* T_s values were calculated using a tipping curve for part of the dataset involving Ceduna.

- Tied array phase stability: Instability in the Narrabri tied array antenna phases, particularly at the higher frequency of 8.4 GHz, occasionally caused spurious variations in correlated amplitude on baselines including Narrabri, in which case data were discarded.

The sparse (u, v) coverage afforded, with only four antennas available in most sessions, means source structure is poorly constrained even when all data are of high quality. Losing data from one antenna considerably reduces the amount of information present! However, following the mantra "bad data are worse than no data",[2] unreliable data are generally removed, as they may lead to substantial errors in modelled source parameters, *particularly* when there are only a small number of antennas. For the sources observed here, which are all strong and compact on LBA baselines, errors can usually be estimated quite well from the internal scatter in the data. Comparing results from session to session is also helpful in error estimation. For data presented here, amplitude errors may be up to $\sim 10\%$, but can be substantially lower in optimal conditions.

Calibration relative to the ATCA

As outlined in Section 2.4.3, it is possible to calibrate the LBA flux density scale by observing a source which is unresolved both at the ATCA and the LBA, with no flux density on intermediate scales. The ATCA flux densities, from the simultaneous observations, are calibrated to an accuracy of typically $\sim 2\%$ against the flux density

[2] private communication from M. H. Cohen to D. L. Jauncey, and thence to the author, as "Bad data are worse than no data at all, but good data are like the cool evening breeze".

of PKS 1934−368. PKS 0537−441 and PKS 1921−293 had been previously found to be very compact, with most of their total flux density seen on the shortest LBA baseline, Narrabri to Mopra. In fact, many of the target sources were found to be at least as compact as these two "calibration" sources. In particular, PKS 1921−293 is noticeably resolved, however it does have a very strong, compact core and is useful as an initial "fringe-finder" for setting up at the correlator. PKS 1519−273, a very compact source which is also known to scintillate strongly, was assumed to be unresolved on all Australian baselines, and was used to determine time-independent antenna gain correction factors for each observation. The intraday variability of PKS 1519−273 does not affect the calibration, since the ATCA observations are simultaneous with the VLBI. The rapidly variable component is unresolved even on VLBI baselines, so that for a given scan, the flux density is the same at both arrays. The correction factors determined were included in the files read by AIPS task ANTAB. After calibration, the data were exported into Difmap for editing and further processing.

Model-fitting and phase self-calibration

At this stage, while the visibility amplitudes are calibrated to 5-10% accuracy, there are still uncorrected errors in the visibility phase, which are determined using phase self-calibration, as discussed in Section 2.2.3. In all cases, a point-source starting model was assumed, which is usually a good starting model for these compact sources. An iterative process of model-fitting and phase self-calibration was used to fit the data. Because of the generally sparse (u, v) coverage and lack of detectable structure, only simple models were fitted - in most cases a single component, as described in Section 3.3.4 below. Where (u, v) coverage was sufficient for imaging, an iterative procedure of phase self-calibration and CLEANing was used. The general procedure for imaging was to deconvolve a small region containing the brightest pixel in the *dirty map*, then subtract the updated model to show up other bright residuals in the field, and so on, until no further improvement could be made.

3.3.4 Results

All sources observed were found to be mostly unresolved on the Australian baselines, as shown in Table 3.6, which lists the average visibilities measured with the LBA for each source. The visibilities are shown as the ratio of the calibrated flux density seen on LBA baselines, to the "total" flux density, as measured simultaneously with the ATCA. This ratio indicates how strongly "core-dominated" the sources are. The ratio may vary somewhat from epoch to epoch, because if, for example, the flux density of the compact component increases significantly, then the ratio of the "core" (LBA) to total (ATCA) flux density will also increase. The rms variation of the ratio for each source measured in different epochs, which is a combination of measurement errors and real variation in "core dominance", is also indicated in Table 3.6. Within the estimated calibration errors, the flux density *difference* between the ATCA and the LBA measurements remains constant, even though the total flux density may vary substantially, i.e. as

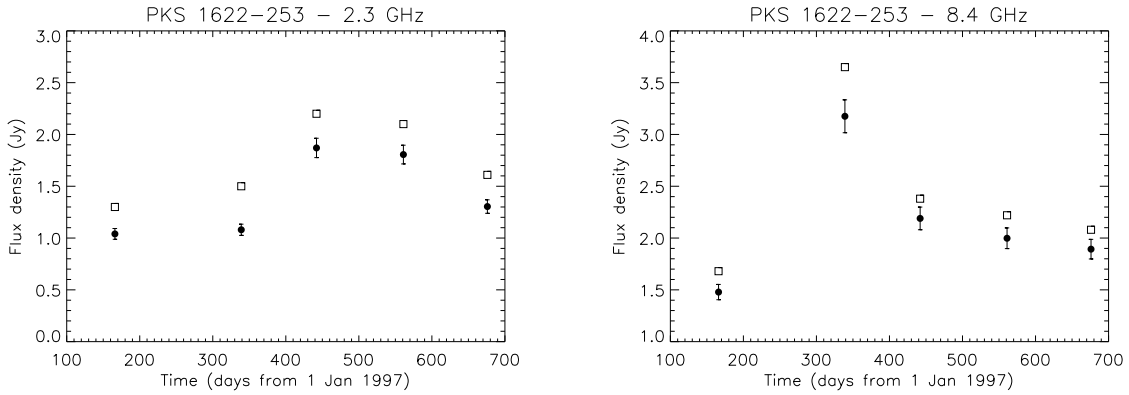

Figure 3.7: LBA (filled circles) and total ATCA (squares) flux density measurements for PKS 1622−253, showing that within the estimated errors, the difference between the two measurements in each epoch, corresponding to the amount of flux density resolved by the LBA, is constant for all observations.

expected, all variability occurs in the compact component which is unresolved with the LBA. This is illustrated in Figure 3.7, which shows the unresolved LBA flux density compared to the total flux density measured at each epoch for PKS 1622−253.

The brightness temperature of a source component, at the emitted wavelength in the rest frame of the host at redshift z, is given by (e.g. Bower & Backer, 1998):

$$T_{\rm b} = 1.41 \times 10^9 (1+z) \left(\frac{S}{\rm Jy}\right) \left(\frac{\sigma_1 \sigma_2}{\rm mas^2}\right)^{-1} \left(\frac{\lambda}{\rm cm}\right)^2, \qquad (3.3)$$

where σ_1 and σ_2 are the FWHM angular sizes along the component's major and minor axes, S is its measured flux density, and λ is the observed wavelength.

Since the sources are all unresolved or barely resolved on Australian baselines, only lower limits on source brightness temperature can be calculated, using model components fitted to the data. The results are shown in Tables 3.7 and 3.8, with the sources modelled as follows.

Where no change in visibility amplitude is evident across the whole (u, v) range, the source is considered unresolved. An upper limit on source size was then estimated by comparing modelled visibilities, assuming a circular gaussian source brightness distribution, with the data. As the modelled source size is increased to a subtantial fraction of the beam, the visibility amplitude drops off toward longer (u, v) spacings. At a distance of 10 Mλ, which corresponds to the typical maximum baseline (Narrabri to Hobart) for the 2.3 GHz LBA observations, and for a circular gaussian source of FWHM size 4 mas, the amplitude is reduced to 88% of the total flux density. 12% is larger than the estimated systematic errors in nearly all cases. For a source of FWHM 5 mas, the amplitude is reduced to 80% of the maximum at a (u, v) distance of 10 Mλ. 5 mas corresponds to 25% of the half-power beam width, and this was taken as a conservative upper limit on source size, for the purpose of calculating a lower limit on source brightness temperature. Following a similar argument, the upper limit on the size of an unresolved source at 8.4 GHz is ~ 1.3 mas.

Table 3.6: Mean visibilities for all sources observed with the LBA, averaged over all epochs, indicating source compactness. The values given are the ratio of LBA visibility amplitudes to total flux density measured simultaneously with the ATCA, $\pm\sigma$, where σ is the rms scatter in the values for different epochs. For each frequency, a visibility $S_{\rm LBA}/S_{\rm tot}$ is given for the shortest and longest Australian baselines, with the approximate baseline length in mega-wavelengths (Mλ) indicated at the top of each column. Source strength is also indicated by the mean total flux density from the simultaneous ATCA data at each frequency, $S_{\rm tot}$.

Source	2.3 GHz			8.4 GHz		
	$\langle S_{\rm tot}\rangle$	$\langle S_{\rm LBA}/S_{\rm tot}\rangle$		$\langle S_{\rm tot}\rangle$	$\langle S_{\rm LBA}/S_{\rm tot}\rangle$	
	(Jy)	~ 1 Mλ	~ 10 Mλ	(Jy)	~ 3 Mλ	~ 40 Mλ
0048−097	0.94	0.90 ± 0.03	0.89 ± 0.03	1.3	0.9 ± 0.1	0.9 ± 0.1
0208−512	3.5	0.91 ± 0.02	0.85 ± 0.02	2.6	0.91 ± 0.05	0.8 ± 0.1
0420−014	2.3	0.96 ± 0.04	0.94 ± 0.04	3.3	0.93 ± 0.06	0.78 ± 0.07
0537−441[a]	2.6	0.95 ± 0.07	0.86 ± 0.05	4.0	0.94 ± 0.05	0.8 ± 0.1
1144−379	1.4	0.97 ± 0.05	0.95 ± 0.05	2.7	0.97 ± 0.06	0.97 ± 0.06
1519−273[b]	1.4	0.98 ± 0.02	0.98 ± 0.02	1.7	1.00 ± 0.00	1.00 ± 0.00
1622−253	1.7	0.81 ± 0.06	0.8 ± 0.1	2.4	0.90 ± 0.02	0.89 ± 0.03
1741−038	2.8	0.98 ± 0.06	0.97 ± 0.06	5.2	0.97 ± 0.02	0.97 ± 0.02
1921−293[a]	13	0.96 ± 0.05	0.72 ± 0.04	14	0.92 ± 0.05	0.73 ± 0.06
1933−400	0.92	0.97 ± 0.05	0.9 ± 0.1	0.89	0.94 ± 0.04	0.86 ± 0.05
2005−489	1.3	0.87 ± 0.07	0.8 ± 0.1	1.2	0.80 ± 0.06	0.76 ± 0.05
2149−306	1.6	1.04 ± 0.09	0.99 ± 0.03	1.5	0.98 ± 0.01	0.98 ± 0.01
2155−304	0.43	0.87 ± 0.09	0.8 ± 0.1	0.40	0.88 ± 0.05	0.84 ± 0.03
2243−123	2.1	1.1 ± 0.1	0.83 ± 0.08	2.1	0.91 ± 0.02	0.62 ± 0.09

[a] Observed as a fringe-finding/calibration source

[b] 8.4 GHz flux density scale set in each epoch using this source only, hence no scatter. 2.3 GHz flux density scale set using average of several sources.

Table 3.7: Models fitted to the central source component, or source size upper limits, and brightness temperature lower limits, from data at 2.3 GHz on Australian baselines. Flux density given is the average over all epochs.

Source	Flux density (Jy)	Major axis (mas)	Axial ratio	PA (N→E) (°)	Min. $T_{\rm b}$ ($\times 10^{10}$ K)
0048−097	0.9	< 5	1	0	$1(1+z)^a$
0208−512	3.0	4.5	0.9	30	8
0420−014	2.2	< 5	1	0	4
1144−379	1.3	< 5	1	0	3
1519−273	1.4	< 5	1	0	$1(1+z)^a$
1622−253	1.4	< 5	1	0	2
1741−038	2.7	< 5	1	0	5
1933−400	0.9	10	0.5	−60	1
2005−489	1.0	< 5	1	0	1
2149−306	1.6	< 5	1	0	5
2155−304	0.4	< 5	1	0	0.4
2243−123	2.0	7	1	0	2

[a] z unknown, hence the factor $(1+z)$ in $T_{\rm b}$

Some sources, for example PKS 1622−253, show an unresolved VLBI component but with some of the total flux density missing. Such sources may contain structure on angular scales intermediate between the ATCA and LBA, of order $0.1 - 5''$ at 2.3 GHz, or $\sim 0.03 - 1''$ at 8.4 GHz. From the ATCA data it is evident that PKS 1622−253 has significant arcsecond-scale structure (see Figure 3.2), which would account for most of the flux density "missing" from the LBA data. The LBA data can be adequately modelled as an unresolved component containing 80% of the total source flux density at 2.3 GHz, and 90% of the total flux density at 8.4 GHz.

A few sources show a drop-off in amplitude towards longer baselines, indicating that the source is partially resolved. In this case, a circular or elliptical gaussian model was fitted to the data. This again gives a lower limit on brightness temperature, since the source may in fact consist of a very compact component plus a weaker, extended component. In the case of an elliptical rather than a circular component, two extra parameters are involved - the axial ratio and position angle of the major axis. For a barely resolved source, the fitted position angle may be a function of the (u, v) coverage rather than any intrinsic source property. Small amplitude errors can alter the fitted position angle. Where there are not enough data to constrain an ellipse, a circular model has been used, i.e. the axial ratio is fixed to a value of 1. PKS 2005−489 visibilities at 2.3 GHz show a sharp drop-off in amplitude from short to medium (u, v) spacings, but level out at larger (u, v) distance. This source is best fitted at 2.3 GHz by a two-component, "core-halo" model, with most flux density in an unresolved core, and ~ 300 mJy in an extended halo. Only the strong, high brightness temperature component is shown in Table 3.7.

Table 3.8: Single component models, or source size upper limits, and brightness temperature lower limits, from data at 8.4 GHz on Australian baselines. Flux density given is the average over all epochs.

Source	Flux density (Jy)	Major axis (mas)	Axial ratio	PA (N→E) (°)	Min. $T_{\rm b}$ ($\times 10^{10}$ K)
0048−097	1.2	< 1.3	1	0	$1(1+z)^a$
0208−512	2.2	3	0.4	60	2
0420−014	3.1	1.5	1	0	5
1144−379	2.6	< 1.3	1	0	6
1519−273	1.7	< 1.3	1	0	$2(1+z)^a$
1622−253	2.2	< 1.3	1	0	4
1741−038	5.0	< 1.3	1	0	10
1933−400	0.8	< 1.3	1	0	2
2005−489	1.0	1.7	0.6	40	1
2149−306	1.5	< 1.3	1	0	5
2155−304	0.4	1.3	1	0	0.5
2243−123	1.9	2.0	1	0	1

[a] z unknown, hence the factor $(1+z)$ in $T_{\rm b}$

The two observing sessions in 1999 which included the Hartebeesthoek antenna provide much higher angular resolution and hence allow measurement of higher brightness temperatures, although the (u, v) coverage is sparse because of the lack of intermediate spacings (see Figure 3.6). Models fitted to the data including baselines to Hartebeesthoek are shown in Table 3.9. Brightness temperature limits are typically an order of magnitude higher than those obtained using the Australian baselines alone.

The observations in March 1999 also included the Ceduna antenna. The baselines to Ceduna give slightly higher angular resolution over the other Australian baselines, and more importantly, are east-west baselines, which significantly improve (u, v) coverage. Images made at 8.4 GHz including the Ceduna antenna are shown in Figure 3.8. These images show that the synthesised beam is quite circular, and that both PKS 1933−400 and PKS 2005−489 have exended emission on the scale of a few mas.

3.3.5 VLBA observations of 3 sources

The NRAO's Very Long Baseline Array (VLBA) is a dedicated VLBI array consisting of ten, 25-m diameter antennas. For sources which are visible from the Northern Hemisphere, the VLBA offers better (u, v) coverage and higher resolution than the current LBA.

A VLBA proposal was submitted to observe three sources which had very little or no previously published VLBI data. Only a single epoch of observations was obtained, on 15 January 2000. The three sources observed were PKS 2155−304, a "high-energy peaked" BL Lac object at $z = 0.116$ (Falomo et al., 1993), PKS 2149−306, a quasar

Table 3.9: Models including Hart data at 2.3 and 8.4 GHz. Parameters shown are as for Table 3.7.

Source	Freq (GHz)	Flux density (Jy)	Major axis (mas)	Axial ratio	PA (N→E) (°)	Min. $T_{\rm b}$ ($\times 10^{11}$ K)
0208−512	2.3	2.2	2	0.6	−10	4.4
0208−512[a]	8.4	1.3	5	0.6	90	0.3
		0.8	< 0.2	1	0	7.1
1144−379	8.4	2.9	0.5	0.3	5	14
1933−400	8.4	0.7	0.8	0.3	−6	1.3
2005−489	8.4	0.8	1.1	0.5	16	0.25

[a] "Core-halo" model, with both components coincident

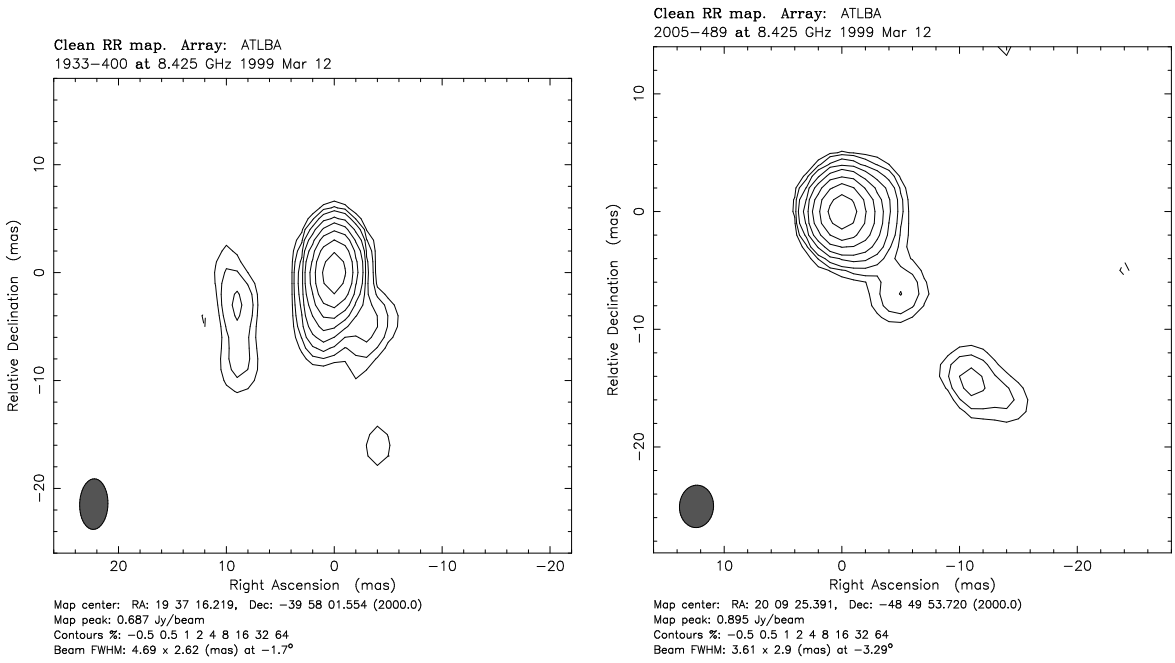

Figure 3.8: Images of PKS 1933−400 and PKS 2005−489 from observations at 8.4 GHz with the LBA including the Ceduna antenna.

Table 3.10: Models from VLBA data for three sources at 2.3 GHz

Source	Flux density (Jy)	Major axis (mas)	Axial ratio	PA (N→E) (°)	Min. T_b ($\times 10^{11}$ K)
2149−306	1.4	1.7	0.6	−50	6.4
2155−304	0.27	0.9	0.6	−7	1.5
2243−123	1.6	3.7	0.3	17	1.5

Table 3.11: Models from VLBA data for three sources at 8.4 GHz

Source	Flux density (Jy)	Major axis (mas)	Axial ratio	PA (N→E) (°)	Min. T_b ($\times 10^{11}$ K)
2149−306	0.9	< 0.2	1	0	14
	0.5	0.6	0.7	−10	1.2
2155−304	0.25	< 0.2	1	0	1.2
2243−123	1.7	1.2	0.1	−3	2.1

at $z = 2.345$, and PKS 2243−123, a quasar at $z = 0.630$. Data reduction for VLBA data is substantially similar to that for LBA data, described in Section 2.4. After calibration and fringe-fitting, data were exported to Difmap for imaging. VLBA data were obtained at 2.3 and 8.4 GHz. Data at 22 GHz were also obtained but were not of usable quality.

Figures 3.9 and 3.10 show the VLBA images obtained for the three sources at 2.3 and 8.4 GHz. PKS 2149−306 has a strong secondary component, 1.1 mas east of the core, which is seen in the 8.4 GHz VLBA data, shown in Figure 3.9. This structure did not show up in the LBA data because of the poor east-west resolution (*cf* Figure 3.6: this source was not observed with Ceduna or Hart in the southern VLBI array). PKS 2155−304 and PKS 2243−123 also have extended emission which could not be modelled with the LBA data.

Component models fitted to the VLBA data, and associated brightness temperature limits, are shown in Tables 3.10 and 3.11. Only the strongest components for each source are shown in the tables. The higher resolution afforded by the VLBA gives brightness temperature limits an order of magnitude higher than those obtained with the LBA, except for those observations which included the Hartebeesthoek antenna in conjunction with the Australian antennas.

3.3.6 Discussion

Clearly, a sparse VLBI array is not ideal for observations of blazars. Although many sources contain a small fraction of their total flux density in extended, arcsecond-scale components, the variability and observable changes in structure occur on milliarcsecond and smaller scales. The Ceduna antenna, which was available for only one of the observing sessions in the present monitoring program, greatly improves the (u, v) coverage of the LBA for imaging. With an improved VLBI array in Australia, including

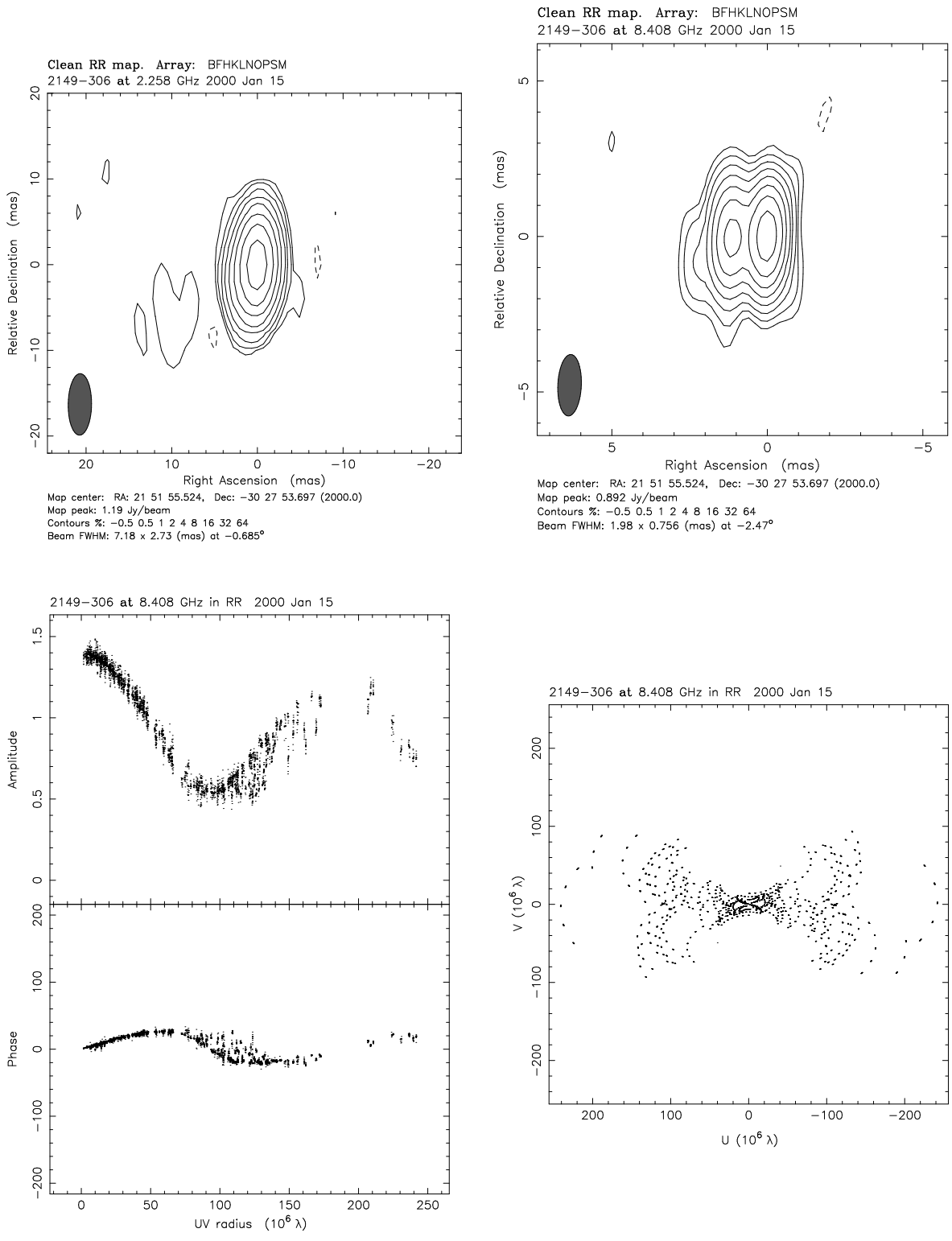

Figure 3.9: VLBA data and images for PKS 2149−306. The upper left panel shows the 2.3 GHz image, and the upper right panel shows the 8.4 GHz image. The (u, v) data at 8.4 GHz are plotted in the lower left panel, and clearly show the "beat" between the two strong components separated by 1.1 mas. The double structure is just resolved with the (u, v) coverage obtained, shown in the lower right panel.

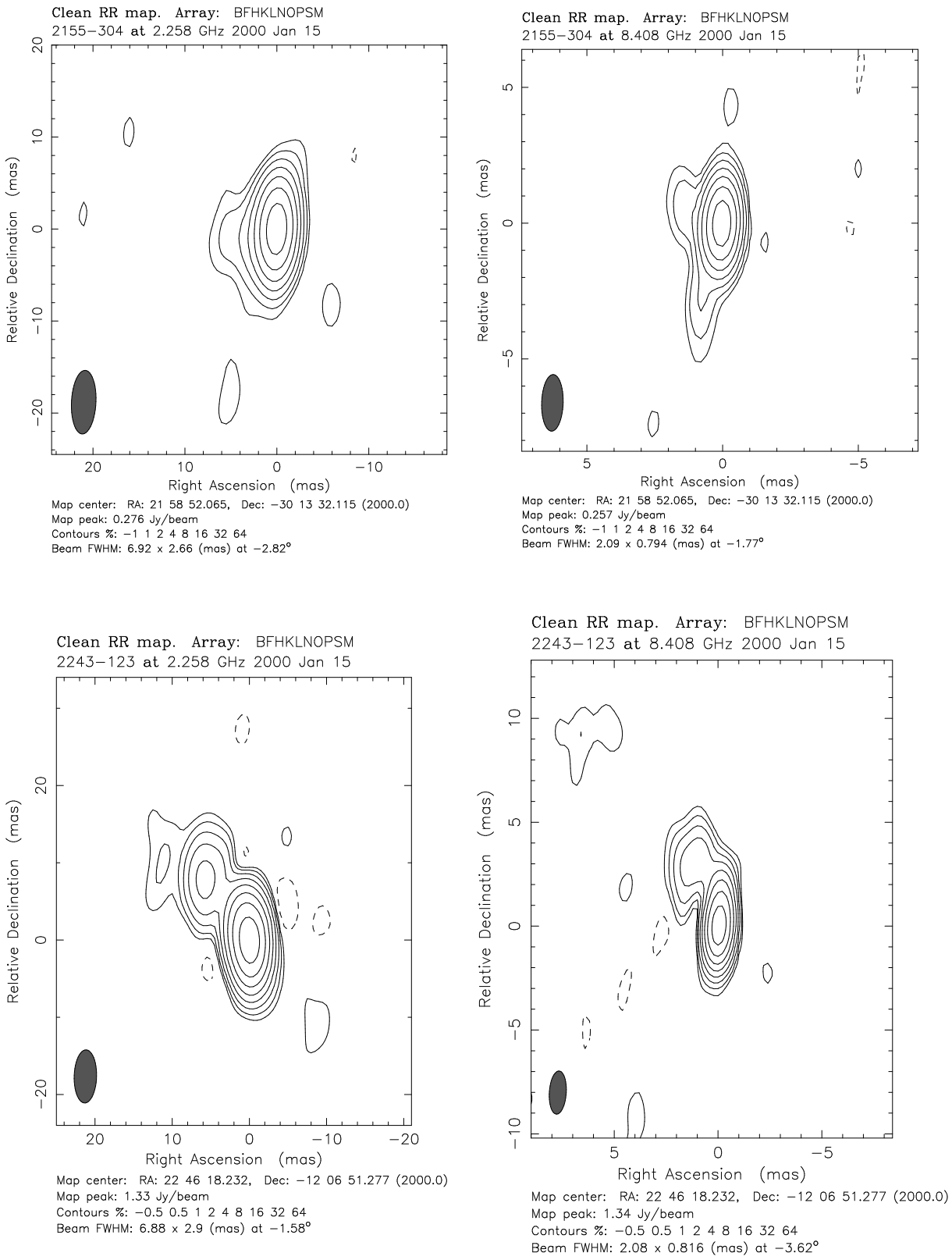

Figure 3.10: VLBA images of PKS 2155−304 (top panels) and PKS 2243−123 (lower panels) at 2.3 and 8.4 GHz.

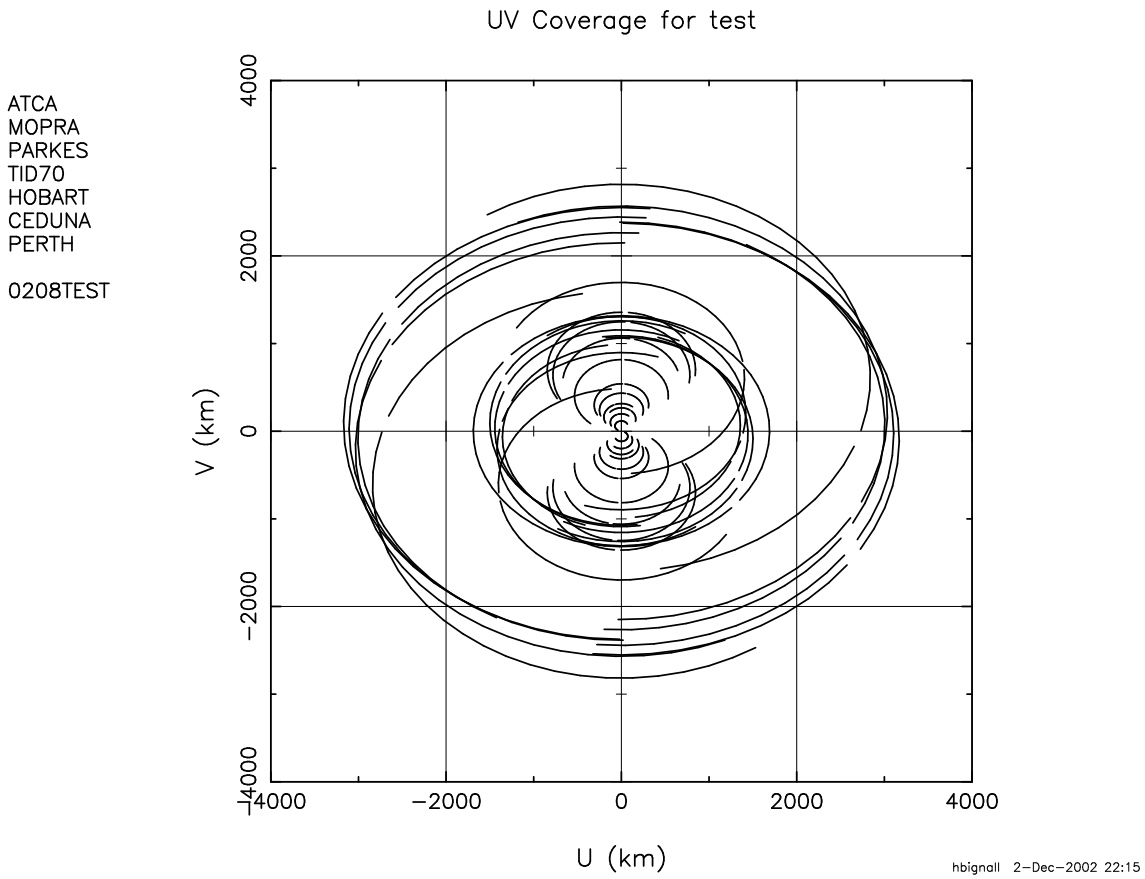

Figure 3.11: The (u, v) coverage which would be obtainable using the Perth antenna in conjunction with the LBA, for a source at $\delta = -51^\circ$

an antenna at Perth, monitoring of changes in source structure on mas scales would be feasible for a number of southern blazars. An example of the (u, v) coverage obtainable using the full LBA plus Perth is shown in Figure 3.11. Higher frequency observations would also give greater resolution, but in general are more difficult to perform and calibrate. There is an important advantage in going to higher frequencies, however — the emitting regions close to the core are more optically thin, and observed ejections of new components, for example, may be more closely related to high energy variability (see, e.g., Valtaoja, 1996). Most of the sources studied here are part of the *International Celestial Reference Frame* (Ma, 1997), and thus high-resolution VLBI monitoring at 2.3 and 8.4 GHz is ongoing.